Surface & Coatings Technology 514 (2025) 132544

Contents lists available at ScienceDirect

Surface & Coatings Technology

journal homepage: www.elsevier.com/locate/surfcoat

Energetic ions for the growth of amorphous and crystalline tungsten-nitrogen layers by HiPIMS

L. Bana [a], D. Vavassori [a,*], G. Marra [b], D. Dellasega [a,c,**], M. Passoni [a,c]

[a] Politecnico di Milano, Dipartimento di Energia, via G. Ponzio 34/3, Milano, Italy
[b] ENI S.p.A. Novara Laboratories (NOLAB), Renewable New Energies and Material Science Research Center (DE-R & D), Via G. Fauser 4, 28100 Novara, Italy
[c] Istituto per la Scienza e Tecnologia dei Plasmi (ISTP) - CNR, via R. Cozzi 53, Milano, Italy

ARTICLE INFO

Keywords:
HiPIMS
Thin film
Transition metal nitride
Microstructure
Synchronized bias

ABSTRACT

This study investigates the deposition of tungsten-nitrogen (WN_x) coatings using high-power impulse magnetron sputtering (HiPIMS), integrating experimental analysis and numerical simulations. We explore how varying N_2/Ar flow ratios and energetic ion bombardment influence coating properties. Specifically, the characteristics of the ion flux impinging on the growing film were controlled by tuning the pulsed bias voltage applied to the substrate in terms of its amplitude and synchronization to the HiPIMS cathode pulse. The nitrogen content of WN_x coatings increases with the N_2/Ar flow ratio but decreases with the bias amplitude. Additionally, the bias synchronization to the main pulse influences film morphology and structure: a bias synchronous to the HiPIMS pulse onset favors β-W_2N crystallization while delayed bias induces film amorphization. Ionization Region Modeling (IRM) simulations of relevant discharges were performed to predict the HiPIMS plasma composition and support the interpretation of experimental results. Findings suggest that precise control over substrate bias in reactive HiPIMS allows to tailor and achieve desired morphological and structural properties of WN_x films.

1. Introduction

In recent years, transition metal nitrides thin films have become critical for different applications, leading to the optimization of their morphological, structural, and functional characteristics. In this context, the case of tungsten-nitrogen mixed layers (WN_x) is particularly interesting. When employed for protective coatings, tungsten nitride in nanocrystalline form exhibits exceptional hardness and wear resistance [1,2]. In the field of microelectronics, amorphous tungsten-nitrogen thin films are employed as copper diffusion barriers thanks to their disordered structure remaining stable during subsequent high-temperature processing [3–5]. In addition, WN_x mixed layers are formed on the surface of tungsten when in contact with reactive environments containing nitrogen. As an example, in nuclear fusion research, the introduction of nitrogen in the edge plasma has been proposed to control plasma-wall interactions by reducing the energy of particles incident on tungsten, the reference plasma-facing material. Under these conditions, the growth of mixed layers containing tungsten and nitrogen is expected on the reactor wall, requiring the investigation of their plasma performance depending on their structure and morphology [6–8].

Due to the variety of applications described for tungsten and nitrogen mixed films, it becomes crucial to tailor their macroscopic properties, including density, hardness, and wear resistance. In turn, these characteristics are determined by the film composition, morphology, and crystal structure. Regarding the latter point, the addition of nitrogen to the bcc crystal structure of α-W either results in a solid solution W(N), or favors the formation of a new crystal structure consisting of an fcc sublattice of W atoms [9]. The octahedral holes in the latter structure can be filled by the nitrogen atoms, with half-filling resulting in the cubic β-W_2N phase, and complete filling giving rise to the hexagonal δ-WN phase. Composition and crystal structure were shown to be directly related to hardness and wear resistance by Polcar et al. [10]. While for a solid solution the nitrogen incorporation increases hardness, the transition to the β phase results in a decrease, though also accompanied by the beneficial effect of lower residual stresses.

To control the microscopic properties of mixed thin films, Physical Vapor Deposition (PVD) techniques are useful tools thanks to the possibility of optimizing growth conditions. A remarkable example is reactive magnetron sputtering (MS), in which the role of working gas pressure and cathode power on the properties of tungsten-nitrogen

* Corresponding author.
** Correspondence to: D. Dellasega, Politecnico di Milano, Dipartimento di Energia, via G. Ponzio 34/3, Milano, Italy.
E-mail addresses: davide.vavassori@polimi.it (D. Vavassori), david.dellasega@polimi.it (D. Dellasega).

https://doi.org/10.1016/j.surfcoat.2025.132544
Received 16 May 2025; Received in revised form 28 July 2025; Accepted 4 August 2025
Available online 6 August 2025

mixed layers has been clarified [11,12]. However, the relatively low adatom mobility during conventional MS processes limited the use of coatings deposited through this method [13]. Indeed, as far as sputtered amorphous WN_x films are concerned, their application as diffusion barrier has been limited by the improved conformal coverage offered by chemical techniques. Moreover, moving to crystalline coatings, the formation of the β-W_2N phase is thermodynamically unfavorable. Therefore, sputter-deposited coatings are prone to develop poor crystalline quality and compressive internal stresses, requiring annealing treatments above 600 °C to improve crystallinity [14–16].

Besides substrate heating, an alternative strategy for controlling thin film growth and properties is energetic ion bombardment [17]. Among the advanced PVD techniques able to supply an ionized matter flux, high power impulse magnetron sputtering (HiPIMS) is steadily growing in popularity because it enables the deposition of high-quality coatings with a dense microstructure [18,19]. HiPIMS is a variant of the more traditional direct current magnetron sputtering (DCMS), applying high voltage pulses to sputter the material cathode at a low duty cycle. While maintaining an average power compatible with the cooling requirements of the cathode, the peak power density can reach values in the range 0.5–10 kW/cm^2, thus generating a high-density plasma and promoting sputtered species ionization.

The ionization of film-forming species by HiPIMS and their energization through substrate biasing have been recognized as effective tools besides substrate heating to control coating growth and characteristics [20–23]. For various transition metal nitrides, including TiN, VN and HfN, HiPIMS enables the production of films with good crystalline quality, compact morphology, and controlled texture, even at room temperature [24–26]. Moreover, heavy metal ion bombardment promotes coating densification, as recently demonstrated for mixed transition metal nitride films by Pshyk et al. [27]. Focusing on the HiPIMS deposition of tungsten nitride, Lou et al. [28] analyzed the role of the nitrogen flow rate on the morphological, structural, and mechanical properties of coatings obtained by superimposed HiPIMS and mid-frequency pulses. In addition, Tiron et al. [6] investigated the plasma irradiation performance of WN_x thin films produced by multi-pulse HiPIMS. However, neither of these recent investigations discussed the effect of ion flux and energy on the thin films properties.

Given the importance of ion bombardment during film growth to control and improve coating properties, understanding the evolution of HiPIMS plasma composition and characteristics is critical. For this purpose, time-dependent global plasma models such as the Ionization Region Model (IRM) are useful tools [29,30]. Specifically, the IRM was recently applied to model the HiPIMS tungsten discharge in argon [31]. In a complementary approach, the model predictions were also exploited to interpret both experimental measurements of plasma properties [32] and the characteristics of HiPIMS-produced tungsten coatings [33]. However, to study tungsten HiPIMS discharge in an atmosphere containing nitrogen, the model must be extended to properly include processes introduced by the reactive gas (e.g., the target poisoning effect [34–36]).

This work investigates the role of energetic ion bombardment in the HiPIMS deposition of WN_x mixed layers by a combined experimental and numerical investigation. The ion flux and energy are controlled by changing substrate bias voltage and timing with respect to the cathode pulse. Regarding numerical simulations, an IRM is developed to describe the HiPIMS plasma time evolution in an Ar/N_2 reactive atmosphere. In light of the results of IRM simulations, coating properties are interpreted and discussed.

2. Methods

2.1. Experimental methods

Tungsten-nitrogen mixed films were deposited onto single side polished 500 μm thick (100) Si wafers cleaned using isopropanol. The HiPIMS equipment used in this work was described elsewhere [37]. Before each deposition, the vacuum chamber was evacuated to a base pressure lower than 5×10^{-4} Pa and then filled with a mixture of Ar (99.999 % purity) and N_2 (99.999 % purity). The chamber pressure was kept constant at 0.5 Pa, while the two inlet gas flows were adjusted to achieve N_2/Ar flow ratio of 10, 25, 50, and 75 %. One cathode was equipped with a circular W target (diameter = 76 mm, thickness = 6 mm) and inclined of 18° with respect to the substrate normal. A dual-channel SIPP2000 generator (Melec GmbH, Germany) was used to power the cathode with HiPIMS pulses of 100 μs length at a duty cycle of 1.75 %. The average power was kept around 230 W. The deposition time was set to 60 min in all cases and, to ensure deposition uniformity, the sample holder was rotated at a uniform speed of 5 rpm in all cases. The sample holder was not intentionally heated during the process. For the case of 50 % gas flow mixture between Ar and N_2, 100 μs-long bias pulses applied synchronously or with a delay of 60 μs with respect to the HiPIMS pulse onset were considered. In both temporal configurations, the bias amplitude was 50 V and 200 V.

The discharge voltage and current waveforms resulting from powering the tungsten cathode with the HiPIMS pulses described above were acquired using a Rigol DS4034 oscilloscope. The concentration of neutral and ionized species was qualitatively assessed by Optical Emission Spectroscopy (OES) measurements in the wavelength interval from 370 nm to 900 nm. For this purpose, in addition to the Ar—N_2 mixtures reported above, two HiPIMS plasmas and two DCMS plasmas ignited in pure Ar and pure N_2 keeping fixed the previously mentioned average cathode power were studied as reference. Film thickness and morphological properties were measured with a Zeiss Supra 40 field emission Scanning Electron Microscopy (SEM), operating at an accelerating voltage of 10 kV. The composition was estimated using an Oxford Instruments Peltier-cooled Silicon drift Detector, combined with the SEM microscope. The film composition was estimated using the Aztec EDS software. A sensitive analytical balance (10^{-5} g) was used to weigh the samples before and after the depositions. Film density was estimated by dividing the deposited mass by the volume, calculated from the deposition area and the average film thickness obtained from cross-sectional SEM images. The crystalline phase of the films was evaluated through X-Ray Diffraction (XRD) analysis in Grazing Incidence geometry, performed using a Panalytical X'Pert Alpha-1 diffractometer with a Cu-Kα source and setting ω equal to 1.0°. XRD peaks were fitted with PseudoVoigt functions [38] to characterize the degree of crystallinity. Although GIXRD is not well suited to assessing texture coefficients of the growing film, we investigated peaks intensity variations to obtain preliminary information on the preferred orientations, following the same approach reported, e.g. by Pandey et al. for AlN [39] and Kumar et al. for SnO_2 [40]. Raman analysis was performed using a Renishaw InVia micro-Raman spectrometer equipped with a diode-pumped solid-state laser (λ = 532 nm) and an 1800 grooves mm^{-1} grating. The laser was focused on the sample through a 50× objective, while the incident power was set to 1 mW. Finally, thermal annealing was carried out on selected samples at 400 °C in a high-vacuum home-made furnace (base pressure 6×10^{-5} Pa, 10 °C/min heating ramp). The nominal temperature was maintained for 2 h.

2.2. Numerical modelling

The Ionization Region Model described in [33] was extended to include plasma and surface processes promoted by the reactive atmosphere. First, six additional populations were included: cold and metastable nitrogen molecules (N_2, N_2^m), molecular nitrogen ions (N_2^+), singly charged nitrogen atomic ions (N^+), cold and hot nitrogen atoms (N^C, N^H). The latter population was included to describe particles back-scattered from the tungsten target at high energy [41]. Preliminary SRIM [42] simulations showed that N ions perpendicularly incident are back-scattered from the surface with a probability of around 30–40 %

and an average energy of approximately 100 eV, considering the discharge voltage set in the 700–900 V range. The reactions relevant for the time evolution of the new populations, along with their energy thresholds and rate coefficients are reported in Table 1.

The target poisoning state is described by means of two additional parameters: the surface (Θ_S) and the bulk compound fraction (Θ_B). Indeed, nitrogen species impacting on a clean W surface are chemisorbed with a sticking probability that strongly depends on the incident energy, surface temperature, and structure [45]. While a value as high as 0.6 was measured for clean (100) surfaces [46], much lower values are found for other crystalline facets [47], therefore motivating the choice of $S_{N2} - W \approx 0.1$. Since atomic species generally have higher sticking coefficients than molecular ones [48], a value of $S_{N-W} \approx 0.5$ was assumed. The nitrogen saturation content on the tungsten surface was estimated from the superficial atom density to be around 7×10^{18} m^{-2} [48]. Moreover, the bulk nitrogen saturation was assumed to be 8×10^{19} m^{-2}, corresponding to a shallow nitrogen implantation of less than 10 nm and limited diffusion [7].

Concerning the sputtering yields as a function of the impacting ion energy, the fits reported by Anders [49] were used for Ar^+ sputtering and self-sputtering yields related to the metallic portion of the target. Instead, always concerning the metallic target, the sputtering yield of N_2^+ and N^+ ions were retrieved from dedicated SRIM simulations. The same was done to estimate the sputtering yield from the poisoned target for all ionized species (Ar^+, W^+, W^{2+}, N_2^+ and N^+), hypothesizing the formation of a WN compound with a density equal to 12.1 g/cm^3 and a binding energy for W and N equal to 7.75 and 5.65 eV [50], respectively. Following [51], the sputtering yield from molecular nitrogen ion impact on both clean and poisoned target regions is computed assuming an equal division of the impact energy between the two nitrogen atoms constituting the molecule.

The secondary electron emission yield γ was obtained from literature data when available. Specifically, for the impact on a clean W surface, a value of 0.02 was reported for N_2^+ and N^+ ions [52,53]. In addition, $\gamma = 0.094$ was proposed for Ar^+ ions [54]. Instead, for doubly charged W ions impacting on the clean W surface, as well as for all ionic species impacting on WN poisoned layer, the correlation originally proposed by Baragiola et al. [55] was adopted. Finally, the effective secondary electron emission yields were calculated as $\gamma_{eff} = \gamma(1 - r)$, with an electron recapture probability $r = 0.7$ [56,57].

Table 1
Reactions involving nitrogen atomic and molecular species implemented in the IRM, along with their energy threshold and rate coefficients, taken from [43]. For hot electron impact reactions, corrections described in [44] were applied.

Reaction	Energy thr. [eV]	Rate coefficient k [m^3/s]
(R1) $N_2 + e \rightarrow N_2^+ + 2e$	15.6	$k^C_{iz,N_2} = k^H_{iz,N_2} = 1.95 \times 10^{-15} T_e^{1.13} \exp(-14.4/T_e)$
(R2) $N_2 + e \rightarrow N_2^m + e$	6.7	$k^C_{ex,N_2} = k^H_{ex,N_2} = 5.81 \times 10^{-15} \exp(-7.57/T_e)$
(R3) $N_2^m + e \rightarrow N_2 + h\nu$	−6.7	$k^C_{ex,N_2} = k^H_{ex,N_2} = 2.3 \times 10^{-4}$
(R4) $N_2^m + e \rightarrow N_2^+ + 2e$	9.43	$k^C_{iz,N_2^m} = k^H_{iz,N_2^m} = 3.39 \times 10^{-13} T_e^{-0.176} \exp(-32.4/T_e)^2$
(R5) $N_2 + e \rightarrow 2N + e$	9.76	$k_{diss} = 6.15 \times 10^{-15} T_e^{0.81} \exp(-12.8/T_e)$
(R6) $N_2^+ + e \rightarrow 2N$	9.76	$k_{diss,2} = 1.9 \times 10^{-15} T_e^{-0.3}$
(R7) $N_2 + e \rightarrow N_2 + e$	–	$k_{el,N_2} = 1.04 \times 10^{-13} T_e^{0.43} \exp(-0.206/T_e)$
(R8) $N_2^m + N_2 \rightarrow 2N_2$	−6.17	$k_{N_2^m - N_2} = 3.5 \times 10^{-18}$
(R9) $N + e \rightarrow N^+ + 2e$	14.54	$k^C_{iz,N} = k^H_{iz,N} = 3.84 \times 10^{-15} T_e^{0.92} \exp(-12.1/T_e)$
(R10) $N + e \rightarrow N + e$	–	$k_{el,N} = 2.18 \times 10^{-13} T_e^{-0.84} \exp(-0.685/T_e)$
(R11) $Ar^+ + N_2 \rightarrow Ar + N_2^+$	–	$k_{Ar^+ - N_2} = 1.2 \times 10^{-17}$
(R12) $N_2^m + N \rightarrow N_2 + N$	–	$k_{N_2^m - N} = 4 \times 10^{-17}$
(R13) $N_2 + N^+ \rightarrow N_2^+ + N$	–	$k_{N_2 - N^+} = 2 \times 10^{-17}$
(R14) $N_2^+ + N \rightarrow N_2 + N^+$	–	$k_{N_2^+ - N} = 1 \times 10^{-17}$

3. Results and discussion

3.1. HiPIMS plasma characterization

Fig. 1a shows the HiPIMS discharge current and voltage waveforms obtained applying 100 μs long pulses at a duty cycle of 1.75 % to a W target in mixed Ar—N_2 atmospheres. In all cases, the discharge voltage waveform exhibits a rectangular shape, while the current increases up to a maximum and then decreases slightly before the pulse termination. The increase in N_2 flow fraction leads to a cathode voltage increase from about 700 V to 950 V, needed to sustain the discharge. Correspondingly, the peak current density decreases from 1.1 A/cm^2 for a pure Ar discharge to 0.7–0.8 A/cm^2 for N_2 rich mixtures. This decrease suggests that a higher reactive gas content limits the ionization efficiency during the HiPIMS pulse. As described in Section 2.1, a fixed average cathode power of 230 W was adopted, resulting in a constant peak power density of 0.7 kW/cm^2.

Fig. 1b reports the Optical Emission Spectra of the HiPIMS plasmas obtained with different Ar—N_2 gas mixtures. For comparison purposes, spectra obtained from DCMS plasmas at similar average power in pure Ar and N_2 are reported. The spectra can be roughly divided into three main regions. First, from 365 nm to approximately 550 nm almost all the peaks correspond to emissions from neutral and ionized W species. Notable exceptions are the two prominent emissions from nitrogen molecular ions (N_2^+) at 391 nm and 427 nm. The second region extends from around 550 nm to 800 nm, where molecular nitrogen (N_2) transitions are mainly observed. Partially superimposed is the third sector, extending from around 750 nm to 895 nm. In this part of the spectrum, mainly Ar and Ar^+ lines are found, together with a prominent peak at 870 nm corresponding to atomic Nemissions.

Comparing the spectra measured in all the HiPIMS plasmas with those obtained in DCMS for pure gases, the latter mainly consists of lines from working gas species (respectively argon and nitrogen), while the former are dominated by emissions from tungsten neutrals and ions. Specifically, in the long wavelength region, the atomic N peak around 870 nm progressively increases with the N_2 flow fraction in HiPIMS. However, in the central region, molecular N_2 bands are almost fully suppressed in all gas mixtures in the HiPIMS regime. Fig. 1c reports a detailed view of the low wavelength interval of the spectra, normalized to their area for comparison purposes. In this spectral region, the peak from N_2^+ at 391 nm grows with the N_2 flow fractions, especially when compared to the decreasing W peak at 429 nm. However, even with a 75 % N_2 flow, the N_2^+ peak intensity remains lower than that observed in DCMS plasmas. This observation suggests a strong gas rarefaction effect in HiPIMS, with the intense sputtering and ionization of tungsten leading to a depletion of neutral gas species in the ionization region, where the optical emission is collected. As a result, the local concentration of molecular nitrogen is reduced, limiting the formation and excitation of N_2^+ ions. In contrast, the progressively increasing atomic N peak at 870 nm indicates that the HiPIMS regime favors the production of atomic species over molecular ions. This trend, specific to the HiPIMS regime, indicates that poisoning of the target surface occurs more gradually compared to DCMS.

The described dependence of current waveforms and OES spectra on the N_2 flow percentage could be described by an increasing yet incomplete target compound coverage during HiPIMS processing under the conditions adopted in this work. It is worth noting here that these observations are contrary to the previous report by Lou et al. [28]. Indeed, they found a triangular current waveform for all plasma compositions, and a prominent N_2^+ peak at 391.4 nm in spectra measured for N_2-rich

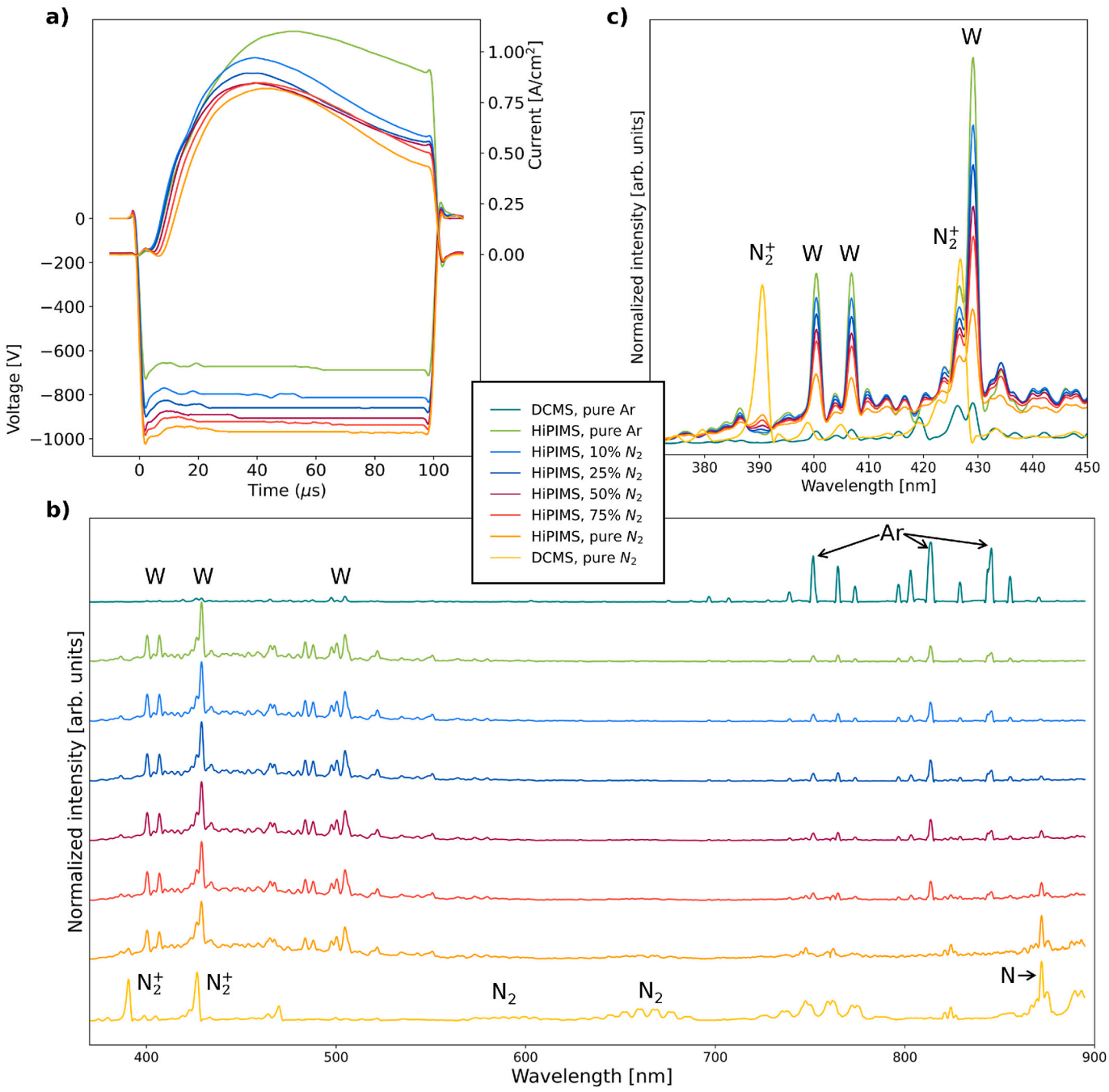

Fig. 1. a) Time evolution of the HiPIMS discharge voltage and current density waveforms of a W target in mixed Ar—N_2 atmospheres. b) Optical Emission Spectra acquired in the HiPIMS conditions of panel a), as well as in DCMS pure Ar and pure N_2 atmospheres, at the same average power. c) Magnification of panel b) in the wavelength interval (370–450) nm, with the intensity normalized to the integrated area of the entire spectrum. In panels b) and c), the main optical emission lines are highlighted for clarity.

mixtures, which was related to saturation of all surfaces with nitrogen. This difference may be due to the higher peak current density employed in this work, in otherwise similar discharge conditions. Indeed, considering the 50 % Ar—N_2 mixture, and normalizing the current to the racetrack area, we get ~2 A/cm^2 (compared to ~0.3 A/cm^2). The enhanced target cleaning promoted by the metal ion self-sputtering therefore extends the transition regime to higher N_2 flow fraction, before shifting to a fully compound-covered target.

3.2. Role of the plasma composition on coating features

The HiPIMS discharges in Ar—N_2 mixtures characterized in the previous paragraph were exploited to produce W—N mixed layers. Fig. 2a shows the atomic percentage of nitrogen and oxygen in the coatings, measured by EDX. By increasing the N_2 flow fraction, the stoichiometry of the coating progressively enriches in N, while the O content remains low (around 5 %). Fig. 2b reports the density and deposition rate of the produced layers. While N_2 flow fractions of 10 and 25 % result in highly dense coating (17.3–18.8 g/cm^3), a steep decrease is observed for N_2 flows above 50 % (11.5–11.7 g/cm^3). The deposition rate remains approximately constant for N_2 flow fractions up to 50 % (4.8–5.2 nm/min) and then decreases to 4.2 nm/min for a N_2 flow fraction of 75 %.

Fig. 3 shows the results of the structural characterization of samples

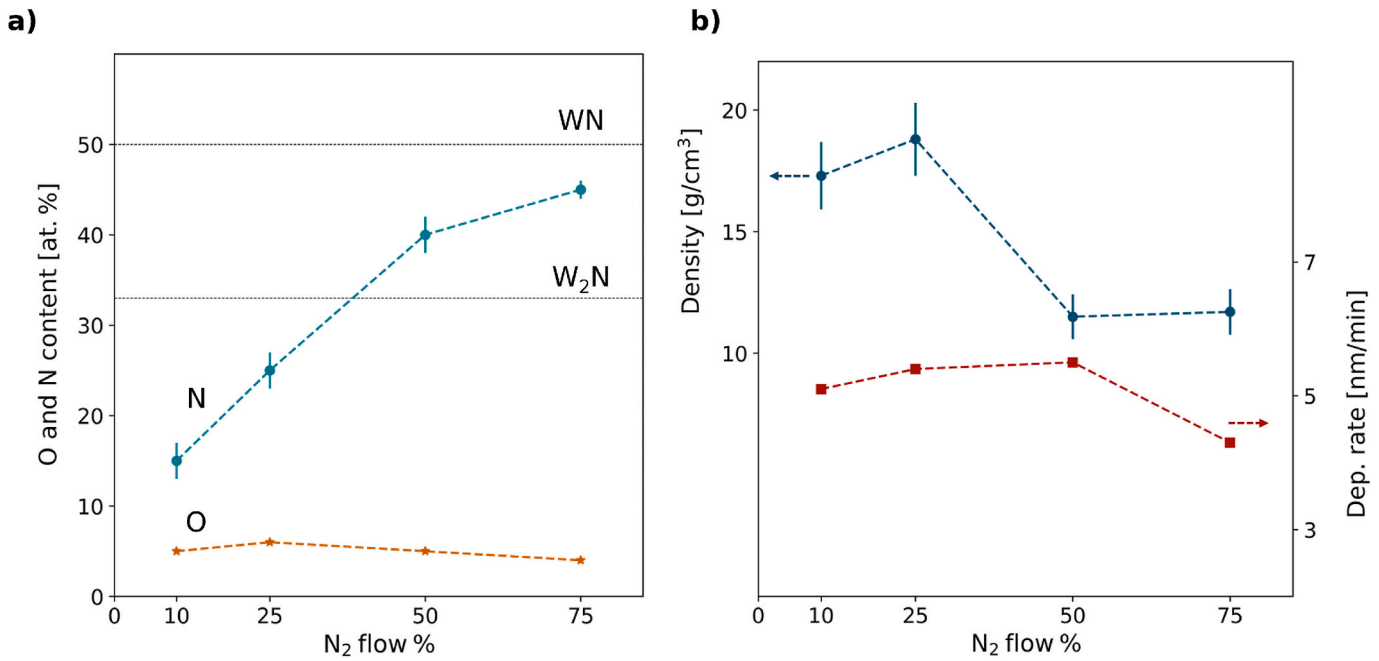

Fig. 2. a) Composition, b) density and deposition rate for W—N mixed layers produced by HiPIMS as a function of the N_2 flow fraction.

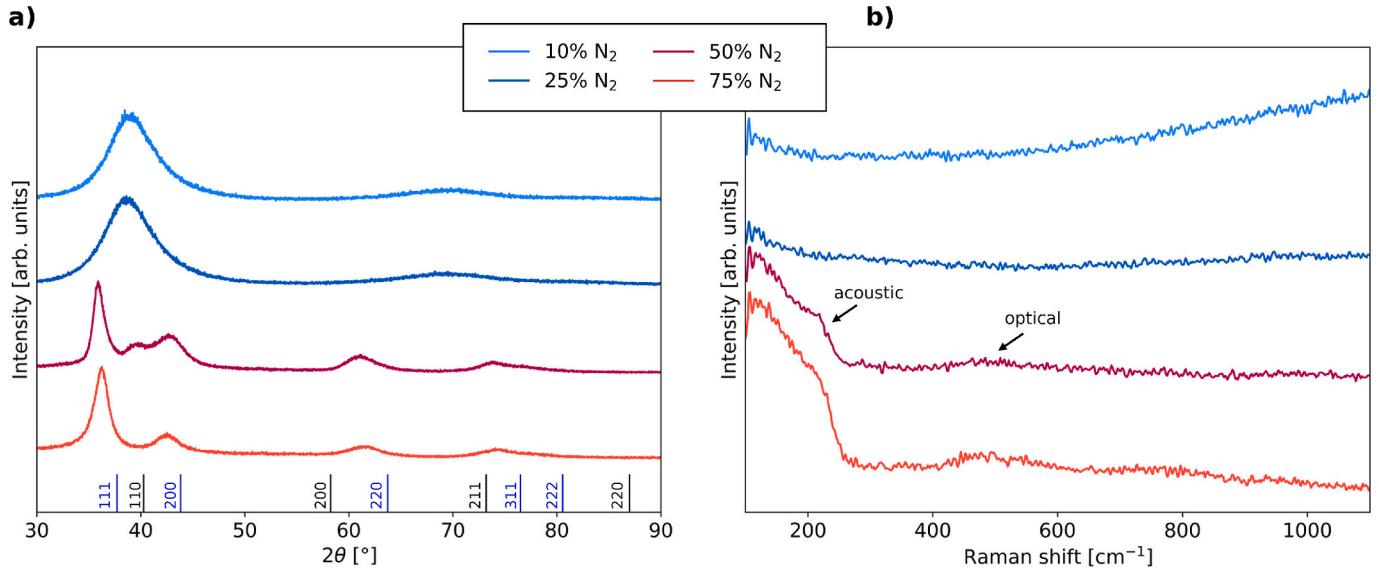

Fig. 3. Structural characterization by a) Grazing Incidence XRD and b) Raman spectroscopy of WN_x thin films obtained by HiPIMS in a mixed atmosphere with N_2 flow fraction of 10 %, 25 %, 50 % and 75 %. In panel a), nominal peak position corresponding to α-W and β-W_2N are shown as vertical black and blue segments, respectively. In both panels, measurements are stacked for clarity.

deposited at different N_2 flow fraction by Grazing Incidence XRD (Fig. 3a) and Raman spectroscopy (Fig. 3b). Concerning the latter technique, it must be emphasized that a perfect fcc β-W_2N structure would not present any Raman active mode. However, breakdown of the translational symmetry due to vacancy defects promotes the appearance of Raman signals resembling the vibrational density of states, i.e. the low-energy acoustic (shift below about 200 cm^{-1}) and the optical band (centered around 470 cm^{-1}) [58]. Ar-rich mixtures (10 % and 25 % N_2) promote an amorphous structure. Indeed, fitting the Principal Diffraction Peaks results in a Gaussian function centered at $2\theta \sim 39.1°$ and 38.8°, with a FWHM of 5.4° and 5.7°, respectively. In both cases, the Scherrer formula predicts a crystallite size of less than 2 nm, which is consistent with amorphous metallic films produced by PVD techniques [59,60]. Coherently, Raman characterization of these samples does not show any signal. Previous works [10,61] have shown that the amorphous structure likely evolves by a progressive disordering of the metastable β-W phase, in turn stabilized by small nitrogen incorporations. In this respect, the progressive displacement of the Bragg peak toward lower angles (larger cubic cell) agrees with an increasing N content trapped in the lattice.

The coating deposited with a 50 % N_2 flow fraction shows a complex structure consisting of amorphous W(N) and β-W_2N phases. Indeed, besides the Principal Diffraction Peak centered at $2\theta \sim 39.7°$, five additional signals compatible with a single fcc β-W_2N structure are observed. The presence of β-W_2N and amorphous W, not predicted by the equilibrium W—N phase diagram at low temperature [7], supports the interpretation of a metastable structure formed under non- equilibrium HiPIMS deposition conditions. Finally, thin films deposited with a

75 % N_2 flow fraction only show the β-W_2N phase signals. In both the latter cases, the diffraction peaks exhibited by the nitride structure are downshifted with respect to their theoretical positions. Specifically, the lattice constant computed from the position of the (111) peak results 4.26 Å for the 50 % case and 4.24 Å for the 75 % case. This indicates a deformation of the structure characterized by an approximate 3 % increase in lattice parameter, caused by excess nitrogen atoms occupying vacant octahedral sites [6,62]. The application of the Scherrer formula to the fitted β-W_2N(111) peak results in a crystallite size of around 6 nm for the 50 % case and 5 nm for the 75 % case. Raman spectroscopy shows an increasing W—N signal for these two samples, confirming the formation of a nanocrystalline, disordered β-W_2N structure. It is worth noting that, despite the presence of up to 5 at.% oxygen in the films (as measured by EDX), no crystalline oxide phases were detected in the XRD patterns or Raman spectra. This suggests that oxygen is either present in amorphous form or incorporated at low concentrations within the nitride matrix without forming separate oxide phases. The EDX results should also be interpreted cautiously, as the technique has limited sensitivity to oxygen in a tungsten-rich matrix, and a contribution from post-deposition surface oxidation cannot be excluded. Fig. 4 displays the SEM cross sectional and planar micrographs of these samples. For a N_2 flow fraction of 10 % and 25 % (Fig. 4a and b), the films grow featureless resulting in a smooth surface with very low contrast at the SEM resolution. On the contrary, when the N_2 flow fraction is increased up to 50 %, a columnar growth typical of Physical Vapor Deposited coatings under low substrate temperature conditions is observed (cf. Fig. 4c), resulting in a surface constituted of nanometric grains. Further grain refinement is observed in Fig. 4d, when the N_2 flow fraction is increased to 75 %.

The deposition of tungsten-nitrogen mixed layers (WN_x) in a HiPIMS plasma under varying N_2 flow fractions revealed a strong correlation between the nitrogen concentration, film morphology, and crystallinity. The nitrogen content in the coatings increases with N_2 flow fraction, reaching nearly 50 at. % for the highest flow rate (75 %). However, the film density decreases sharply beyond 50 % N_2, suggesting a transition in film growth dynamics. Specifically, film structure evolves from amorphous W(N) to nanocrystalline β-W_2N between 10 and 50 % N_2 flow, with a well-defined crystalline phase present above 50 % N_2. Whereas DCMS relies largely on the thermal mobility of neutral adatoms, HiPIMS delivers a sustained flux of metal ions that transfers momentum and energy directly into the near-surface region, promoting localized defect annealing and enhanced surface diffusion even at room temperature. Thus, HiPIMS provides sufficient ion energy to promote crystallization at room temperature with no applied bias.

Compared to the previous report by Lou et al. [28], the higher peak power density described in the previous section may promote an enrichment of the plasma chemistry in the more reactive atomic N compared to molecular species. This hypothesis agrees with measurements of ion energy distribution functions by Tiron et al. [6]. Thus, despite the target remaining in a transition regime, the higher nitrogen incorporation allows the formation of nanocrystalline β-W_2N. These results therefore highlight the importance of controlling the HiPIMS peak cathode power to tune the properties of W—N mixed layers.

3.3. Role of ion energy and flux

As described in the previous section, coatings produced with a N_2 flow fraction of 50 % and a grounded substrate show a metastable structure characterized by a mixture of tungsten nitride and amorphous tungsten. In this section, the effect of the incident ion energy and flux is studied for this case by changing the substrate bias voltage and time delay with respect to the HiPIMS cathode pulse onset. To assess the role of thermally activated diffusion processes in the absence of energetic bombardment, we annealed a film deposited with a 50 % N_2 flow fraction and grounded substrate at 400 °C for 2 h. These conditions were chosen to induce atomic diffusion but remain below that required to achieve β-W_2N crystallization, about 470 °C [62]. While annealing primarily activates bulk diffusion, this comparison provides a

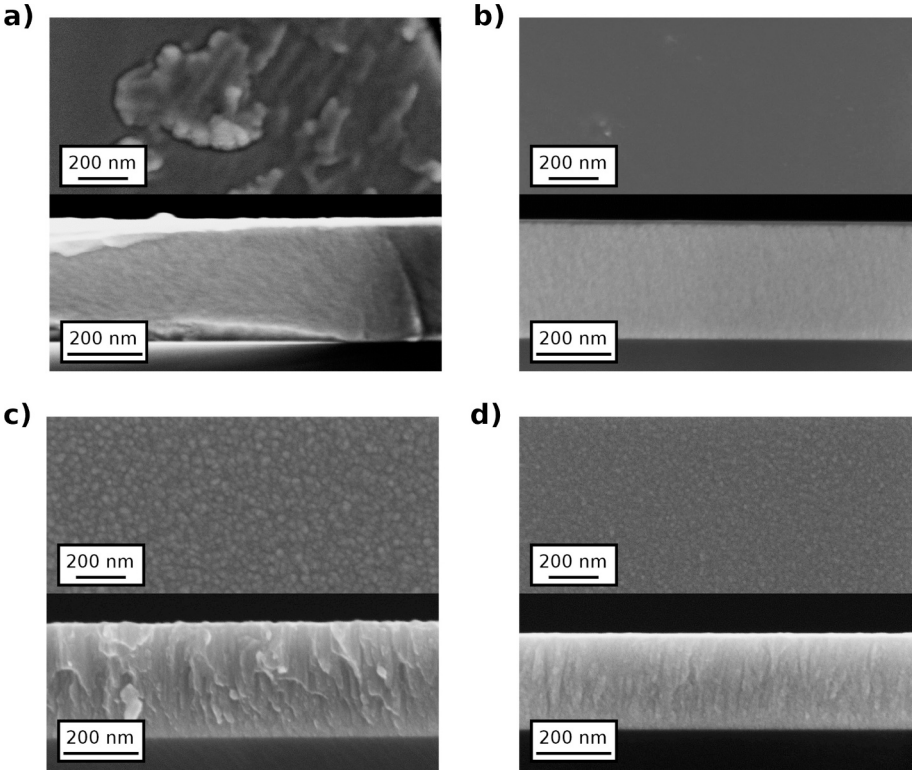

Fig. 4. SEM cross sectional and surface micrographs of W—N thin films obtained by HiPIMS in a mixed atmosphere with N_2 flow fraction of a) 10 %, b) 25 %, c) 50 % and d) 75 %. For each panel, the upper images show planar SEM views, while lower images correspond to cross sectional views.

qualitative reference to distinguish thermal effects from those induced by energetic ion irradiation during deposition.

Table 2 summarizes the bias configurations adopted to obtain the samples described in this section, as well as the resulting stoichiometry and density. Samples produced with a 50 V bias result slightly over-stoichiometric with respect to the expected W_2N phase, similarly to the coatings obtained under grounded conditions described in the previous section. On the contrary, the application of 200 V bias pulses reduces the nitrogen content in the film because of preferential sputtering consequence of the lower surface binding energy of the nitrogen atom [63].

Fig. 5 shows the results of the structural characterization of samples produced in a mixed atmosphere with a N_2 flow fraction of 50 % and different bias configurations. Specifically, Grazing Incidence XRD and Raman measurements are reported in Fig. 5a and b respectively. The application of a 50 V bias, both synchronized and delayed with respect to the pulse onset, makes the broad α-W diffraction band observed in the grounded substrate case (cf. Fig. 3a) disappear, resulting in a single polycrystalline fcc β-W_2N structure. Fitting the (111) peak for the sample produced with synchronized bias yields a FWHM of 1.7° corresponding to a crystallite size of approximately 4 nm. A better crystalline quality (FWHM of 1.3° and domain size of 7 nm) is observed for the delayed bias case. Accordingly, Raman measurements show an attenuated acoustic and the absence of the optical band, representative of an improved crystalline quality (cf. Fig. 5b and Fig. 3b).

Increasing the bias to 200 V, the structure markedly depends on the biasing configuration with respect to the HiPIMS pulse. Specifically, 200 V bias synchronized to the pulse onset results in a relative increase of the (111) signal intensity. The main diffraction peak is centered at $2\theta = 37.04°$ with FWHM of 0.77°, yielding a crystallite size of 12 nm. Finally, the application of a 200 V delayed bias results in a diffraction band centred at $2\theta \sim 38.18°$ with a FWHM of ~6.4°, corresponding to a crystallite size less than 2 nm. Raman spectroscopy shows an almost complete suppression of the acoustic band, confirming the formation of an amorphous structure.

For comparison, the XRD characterization of annealed samples is also reported in Fig. 5a. The wide band centered at $2\theta \sim 39.7°$ has disappeared upon annealing the sample, leading to a single β-W_2N structure characterized by a partial recovery of the peak downshift. The crystallite size, estimated applying the Scherrer formula to the (110) peak, results 7 nm. Moreover, the intensity of the (200) diffraction peak increases compared to the (111) signal. Comparing the intensity ratio $I_{(200)}/I_{(111)}$, an increase from 0.73 (similar to the expected value of 0.66 for the bulk material) to 1.08 is observed upon annealing. As previously reported by Shen et al. [14], this could be associated with an orientation selection along the (100) direction upon annealing, although additional measurements (e.g., pole figures) would be helpful to further clarify these findings.

The morphological characterization of the coatings obtained under different biasing conditions is reported in Fig. 6. The application of 50 V bias pulses, both synchronized and delayed with respect to the pulse onset (Fig. 6a and b), promotes the development of a more regular columnar morphology, with vertically aligned and denser columns compared to the floating potential case (cf. Fig. 4c). SEM micrographs in Fig. 6c highlight that with a synchronized 200 V bias, the film exhibits a layered structure with a transition from an initial featureless growth to a columnar one. In contrast, Fig. 6d shows that a 200 V bias applied with a 60 μs delay produces a disordered, granular morphology, demonstrating how both ion energy and bias timing influence the film growth and microstructure.

Table 2
Samples produced under 50 % N_2 flow fraction and different bias configurations discussed in Section 3.3, along with their stoichiometry measured by EDX and density.

Bias		Composition [at. %]			Density
Configuration	Voltage [V]	N	O	W	[g/cm^3]
Sync to pulse onset	50	40	3	56	13.5
60 μs delay	50	37	4	58	13.7
Sync to pulse onset	200	30	4	66	13.1
60 μs delay	200	30	5	65	16.5

The results presented in this section demonstrate the possibility of controlling morphology and structure of mixed tungsten and nitrogen thin films produced by HiPIMS with the application of a pulsed bias, synchronized or delayed with respect to the cathode pulse onset. Specifically, bombardment with low energy ions (50 eV) under our experimental conditions improves the film crystallinity, causing an increase of the (111) peak intensity. Similarly, crystallization from an amorphous W (N) to an fcc β-W_2N phase was obtained by moderate biasing in DCMS depositions by Guruvenket et al. [64]. However, the excessive Ar incorporation resulting from gas ion bombardment in biased DCMS can degrade thermal and mechanical properties.

Finally, high voltage substrate bias in HiPIMS further improves the crystallinity or induces amorphization, depending on the bias synchronization with respect to the cathode pulse onset.

The ability to tailor film structure from nanocrystalline β-W_2N to fully amorphous through precise control of substrate bias and pulse timing is a crucial aspect for application-specific coating optimization. Specifically, compact amorphous layers based on tungsten are particularly attractive for diffusion barrier and corrosion-resistant coatings in liquid-metal environments due to their isotropic structure and lack of grain boundaries [65]. For wear-resistant coatings, the compact, nanocrystalline β-W_2N allowed by synchronized bias pulses is particularly desirable due to its high hardness, good adhesion, and wear resistance [10,66]. Finally, in the field of plasma-surface interactions for nuclear fusion, both amorphous and nanocrystalline films have useful features for use as proxy of redeposited tungsten-nitrogen mixed layers [6].

3.4. Model results and discussion

The IRM presented in [33] and extended as described in Section 2 is applied to the tungsten discharge in a 50 % argon-nitrogen mixture to determine the temporal evolution of the plasma properties and composition. Relying on the comparison between the observed current waveforms and OES spectra with the previous data by Lou et al. (cf. Section 3.1), we assume a transition regime for the W target in the HiPIMS conditions analyzed here. The hypothesis of an incomplete target poisoning also agrees with the weak reactivity of tungsten toward nitrogen, as can be inferred by the small enthalpy of formation of the W—N compounds [67]. Therefore, for the discharge in a 50 % argon-nitrogen mixture simulated in this work, an initial value of 0.25 is assumed for both the surface and bulk target poisoning compound fraction (see Section 2 for the definition of these two quantities). The sputtering yields were estimated according to the prescriptions described in Section 2, considering an applied voltage of 850 V during the HiPIMS pulse. The results, used as input for the IRM, are summarized in Table 3.

As discussed in [33], the IRM has two free parameters to fit the modelled current to the one measured during experiments: the ion back-attraction probability β and the voltage drop across the ionization region U_{IR}, represented as a fraction of the discharge voltage U_D according to $f_{PWR} = U_{IR} / U_D$ [68]. The simulation is then optimized by comparing the modelled and experimental current waveforms using a normalized weighted sum of square residuals as a figure of merit [69]. Fig. 7 reports a color map in the plane (β, f_{PWR}) of the mentioned figure of merit. The optimal solutions are found in the darker red region of the map. The black lines represent curves of constant ionized flux fraction (F_{flux}) computed as in [70], and a dashed ellipse was drawn to enclose the (β, f_{PWR}) region of the plane containing the 20 most accurate IRM solutions. While a complete fit requires experimental measurements of the ionized flux fraction in addition to the current time evolution, the most

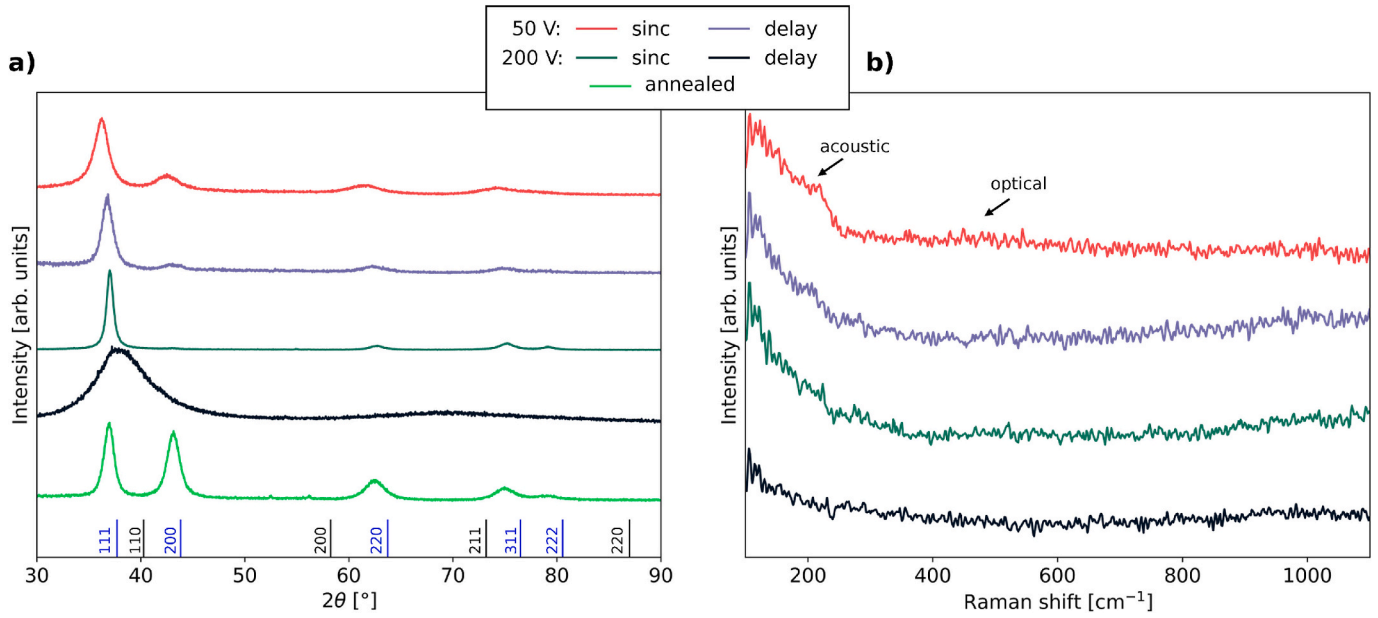

Fig. 5. Structural characterization by a) Grazing Incidence XRD and b) Raman spectroscopy of WN_x thin films produced in a mixed atmosphere with N_2 flow fraction of 50 % and different bias pulse configurations: synchronized to the pulse onset and delayed of 60 μs, with an amplitude of 50 V and 200 V. In panel a, nominal peak position corresponding to α-W and β-W_2N are shown as black and blue vertical segments, respectively.

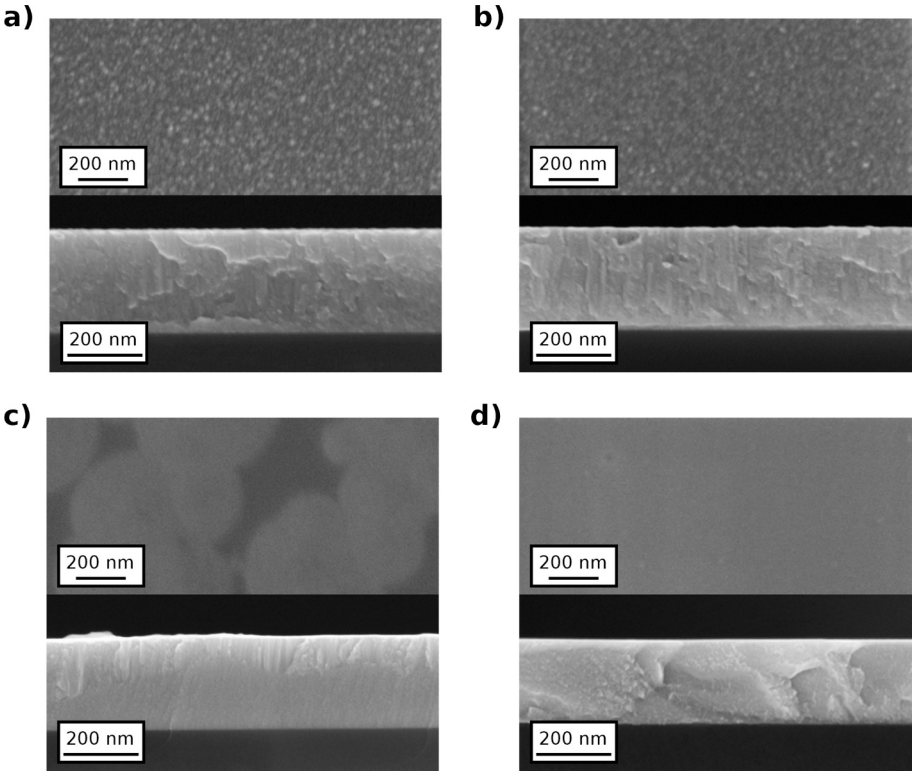

Fig. 6. SEM planar and cross sectional micrographs of W—N thin films obtained in a mixed atmosphere with N_2 flow fraction of 50 % and different bias configurations: a) 50 V synchronized to the pulse onset, b) 50 V delayed of 60 μs, c) 200 V synchronized to the pulse onset, and d) 200 V delayed of 60 μs. For each panel, the upper images show planar SEM views, while lower images correspond to cross sectional views.

significant trends can already be captured by an optimization over the single parameter f_{PWR}. Indeed, as can be seen from the figure, the optimal solutions gather in a specific region of the (β, f_{PWR}) plane, characterized by F_{flux} ranging approximately from 0.34 to 0.43.

The resulting best fit discharge current waveforms are reported in Fig. 7(b) and (c), together with the separate contributions from the electronic and ionic populations according to the IRM. Two optimal solutions are presented corresponding to the extreme values of β in the previously described ellipse. Specifically, the solution with the lowest $\beta = 0.64$ is reported in Fig. 7(b) and the solution with the highest $\beta = 0.70$ is shown in Fig. 7(c). First, the simulated current waveform satisfactorily matches the experimental measurement for both (β, f_{PWR}) couples. The

Table 3
Sputtering yields used as input for the IRM simulations.

Target material	Sputtered species	Bombarding ion				
		Ar^+	N_2^+	N^+	W^+	W^{2+}
W	W	1.44	0.32	0.52	1.19	2.03
WN	W	0.70	0.21	0.34	0.45	0.83
WN	N	0.71	0.25	0.40	0.47	0.82

qualitative time evolution of the current composition also agrees. Indeed, in the first 20 μs, the current is mainly sustained by Ar^+, with a lower contribution by N_2^+ ions. Afterwards, gas rarefaction is observed leading to a decrease in the Ar^+ and especially N_2^+ current. Instead, back-attracted ions of the sputtered species progressively increase, with W^+ ions becoming the dominant species after about 20 μs. Interestingly, the N^+ current remains low and comparable to the W^{2+} one. The low simulated electron density and high temperature (about 8×10^{18} m^{-3} and 7.5 eV during the pulse, respectively) are the main cause of the relevant current contribution of doubly-ionized W ions, contrarily to previous results in pure Ar with similar HiPIMS discharge parameters [33].

Given the consistency observed between the results with different optimal couples (β, f_{PWR}) within the described ellipse, only the best-fit solution corresponding to ($\beta = 0.664$, $f_{PWR} = 0.096$) will be considered in the following. The main outcomes of the IRM for this case are shown in Fig. 8. First, Fig. 8a and b report the time evolution of the particle density. Specifically, Fig. 8a refers to N_2 and Ar species, while 8b pertains to W and N. This classification was adopted to reflect the different particle origin and energy spectrum [18]: plasma processes for Ar, N_2, and their ions, and target phenomena (sputtering) for W species. While atomic N is also supplied by molecular dissociation, its density was reported in Fig. 8b for visualization purposes. After the first 20 μs, gas rarefaction of Ar and N_2 causes the plasma to be mainly composed of N neutral species. W neutral density remains lower than N, peaking at around 7×10^{18} m^{-3}. However, a completely different picture emerges from the analysis of ionic populations (thicker lines in Fig. 8a and b). While at the beginning of the pulse Ar^+ and N_2^+ have the highest density, W^+ rapidly becomes the dominant contributions, peaking at a value of approximately 5×10^{18} m^{-3}. Moreover, the density of W^{2+} species remains approximately one order of magnitude smaller than the singly-charged one and comparable to the N^+ density.

Fig. 8c shows the ionic density fraction in the IR ($F_{dens,i}$, i = W,N) and in the flux entering the diffusion region ($F_{flux,i}$, i = W,N) [70]. The tungsten species are highly ionized for what concerns both their density and flux, with a time-averaged value of 43 % and 39 %, respectively. Even though a non-negligible degree of ionization is found for the flux of nitrogen atomic species, Fig. 8d shows that this flux represents a minor contribution to the total ion flux at the IR borders, dominated by Ar^+ soon after the pulse onset and later by W^+, including the immediate afterglow. Fig. 8e shows the time evolution of the main production and consumption contributions of the N atoms during the HiPIMS pulse. The model highlights the dominant contribution to N production by molecular dissociation, in agreement with previous experimental measurements of HiPIMS discharges in similar systems [71]. Despite the assumption of partial covering of the target surface, sputtering of the compound results a major component to N generation. This observation agrees with mass spectrometry measurements showing an important source of N by surface processes [72]. In this respect, it must be emphasized that future implementations of the IRM should properly account for collisional dissociation of molecular N_2^+ impacting on the

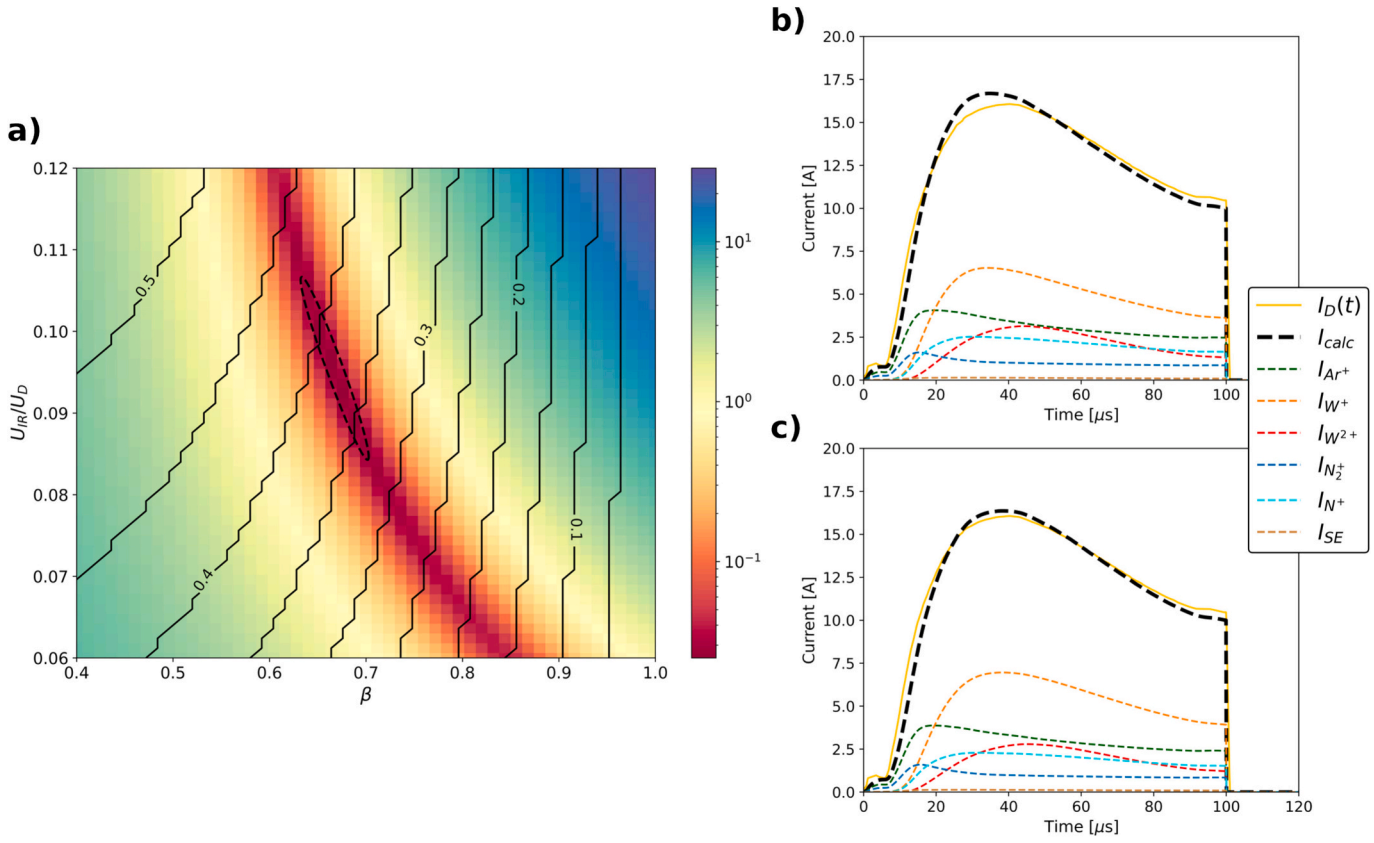

Fig. 7. a) Color map in the plane (β, f_{PWR}) showing the root mean square fitting error between the simulated and experimental current waveforms obtained sputtering a W target in a 50 % argon- nitrogen mixture. The black lines represent curves of constant ionized flux fraction values according to the IRM. b) and c) Fits of the computed discharge current to the experimental one and its composition at the target surface for the fitting parameter couples ($\beta = 0.64$, $f_{PWR} = 0.106$) and ($\beta = 0.70$, $f_{PWR} = 0.085$), respectively.

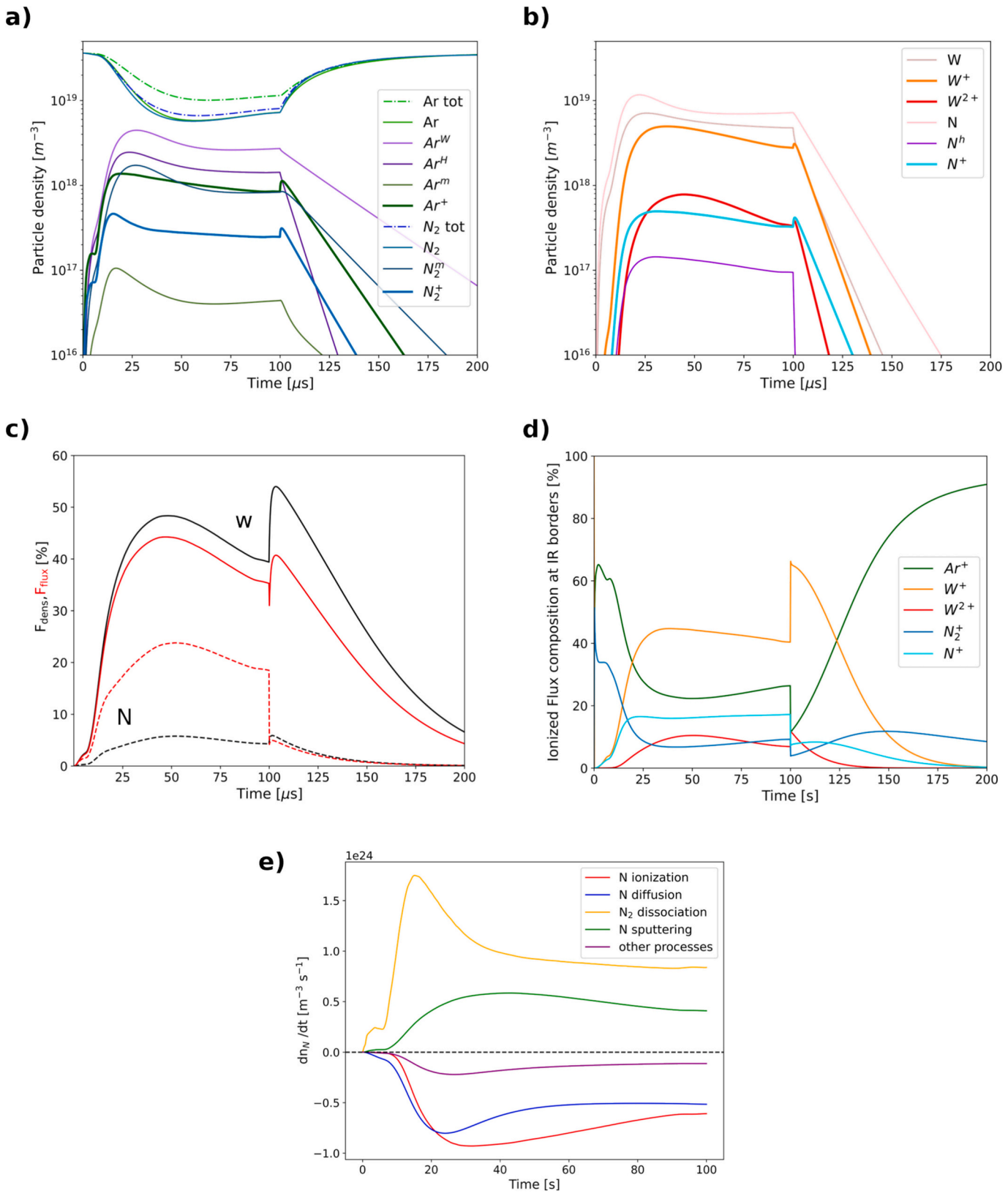

Fig. 8. The time evolution predicted by the IRM of a) Ar and N_2 and b) W and N particle density; c) ionized density fraction (in black) and ionized flux fraction (in red) for W as a continuous lines and N as a dashed lines; d) ionized flux composition at the IR border. e) partial contributions of the main plasma and surface processes to the time derivative of the N atomic density.

target surface.

The numerical results presented in this section allow to discuss further the evolution of morphological and structural coating properties with the ion energetics, controlled by the substrate bias. First, a bias voltage of 50 V results in a columnar growth characterized by a polycrystalline β-W_2N structure, independently on the chosen bias time configuration. In this respect, ion bombardment plays a crucial role in the microscopic processes underlying film growth (i.e., island nucleation, growth, and coalescence) [73]. In our case, the additional energy input provided by the 50 V bias enhances adatom mobility during film growth. As a result, orientation selection mechanisms driven by anisotropies in surface diffusion across crystallographic facets can become active despite the low substrate temperature, leading to a microstructure consistent with zone T in the structure zone diagram [17]. For the fcc β-W_2N phase, the increased intensity of the (111) reflection observed in the XRD pattern of the 50 V delayed bias sample may be related to this process. It must be emphasized here that a bias pulse applied 60 μs after the cathode pulse onset is actually synchronized to the metal-ion rich portion of the discharge, considering the time evolution of the plasma composition presented above and the sputtered particles time of flight from target to substrate. Therefore, the 60 μs-delayed bias configuration provides a more efficient ion bombardment environment compared to the synchronized case, exploiting the high ionized flux fraction in the immediate afterglow.

Moving to the high-energy regime, surface erosion is evident by the thickness reduction in SEM images of coatings produced at 200 V, compared to 50 V and the grounded substrate case. The phenomenon is more relevant for coatings deposited under a delayed bias compared to a synchronized one, which confirms the more efficient ion bombarding due to the increase $F_{flux,W}$ in the immediate afterglow. Moreover, despite a similar stoichiometry, the effect of high-energy ion bombardment on the morphology and structure strongly depends on the bias voltage synchronization to the cathode pulse. The intense flux of high-energy tungsten ions in the afterglow promotes repeated re-nucleation and disruption of local crystal order, leading to nanocrystalline morphology. Argon entrapment in the film may also contribute due to the enhanced ion flux at the IR boundary during the afterglow (see Fig. 8d). On the other hand, moderate ion fluxes during the pulse on-time allow enhanced adatom mobility and film recrystallization. In this respect, the featureless to columnar transition observed at higher thickness could be related to the evolving nature of the growth surface. As deposition progresses, adatoms first diffuse on the bare silicon substrate and then on the previously deposited WN_x film, which offers different surface energetics and bonding conditions. Similar effects have been reported in other material systems [74,75]. Additionally, progressive substrate heating during the deposition and compressive stresses induced by energetic ion flux may also play a role in microstructure evolution.

4. Conclusions

The role of ion bombardment in the HiPIMS processing of tungsten in argon-nitrogen mixed atmosphere was investigated by a combined experimental and modelling approach. Thin films were produced with different nitrogen flow fractions and substrate bias voltages, both in terms of amplitude and synchronization with respect to the main cathode pulse. Morphology, microstructure, composition and density of the grown films were characterized. For the low bias amplitude considered, both timing resulted in a comparable improvement in crystalline quality. On the other hand, for the high bias amplitude, the pulsed bias effect on films properties strongly depends on the onset time delay. Indeed, while synchronized bias favors film crystallization, 60 μs delayed bias can induce amorphization and a featureless morphology.

In addition, the Ionization Region Model (IRM) was successfully applied to the HiPIMS reactive discharge of tungsten in argon-nitrogen atmosphere. First, nitrogen atomic and molecular species, as well as the target poisoning state, were introduced into the model. The time evolution of the plasma composition during the pulse on-time and the afterglow was predicted for an experimental discharge in a 50 % Ar—N_2 mixture. Results show that, while the discharge current is sustained almost equally by Ar^+, W^+, and N^+, the W^+ density is larger than the N^+ density for the whole pulse and during the afterglow.

We demonstrated the effectiveness of an energetic ion flux as a way to control morphology and properties of mixed tungsten-nitrogen thin films as an alternative to post-deposition heat treatments. However, not all the considered ion acceleration schemes allowed crystallization of the β-W_2N phase. Specifically, by applying a bias of 200 V with a delay of 60 μs from the HiPIMS pulse onset, the intense high-energy ion flux in the afterglow causes amorphization of the film through defect generation and continuous recrystallization. Therefore, in the nitrogen-reactive HiPIMS regime explored in this work, the need to synchronize the bias with the metal-rich portion of the pulse (taking into account W^+ ions time-of-flight) is less critical for the production of films of good crystallinity. Additional ion acceleration schemes, such as longer biases or the application of bipolar cathode pulses, remain to be investigated as a future development.

This work shows how a combined experimental and numerical approach can be effective in improving our understanding of the connection between the HiPIMS tungsten discharge characteristics in argon-nitrogen mixed atmosphere and the experimentally observed properties of the deposited films. With reference to MCF research, the presented results could be relevant for the production of W—N mixed layers with tailored structure and morphology for both plasma-wall interaction experiments and as barrier layers against liquid metal corrosion. Future work should be devoted to expanding the ion energy regime and working gas mixtures to refine control over thin-film properties. Additionally, pole figure measurements will improve our understanding of structural features and orientation selection in WNx films. Finally, extending the IRM to account for collisional dissociation of molecular nitrogen ions at the target surface could further enhance predictive accuracy.

CRediT authorship contribution statement

L. Bana: Writing – review & editing, Writing – original draft, Visualization, Methodology, Investigation, Formal analysis, Conceptualization. **D. Vavassori:** Writing – original draft, Investigation, Formal analysis. **G. Marra:** Investigation. **D. Dellasega:** Writing – review & editing, Supervision. **M. Passoni:** Writing – review & editing, Supervision, Resources.

Declaration of competing interest

The authors declare the following financial interests/personal relationships which may be considered as potential competing interests: Matteo Passoni reports financial support was provided by European Consortium for the Development of Fusion Energy. Luigi Bana reports financial support was provided by Eni SpA. If there are other authors, they declare that they have no known competing financial interests or personal relationships that could have appeared to influence the work reported in this paper.

Acknowledgements

This work has been carried out within the framework of the EUROfusion Consortium, funded by the European Union via the Euratom Research and Training Programme (Grant Agreement No. 101052200 — EUROfusion). Views and opinions expressed are however those of the author(s) only and do not necessarily reflect those of the European Union or the European Commission. Neither the European Union nor the European Commission can be held responsible for them.

L. B. acknowledges Eni S.p.A. for funding his PhD program.

Data availability

Data will be made available on request.

References

[1] D. Javdošňák, J. Musil, Z. Soukup, S. Haviar, R. Čerstvỳ, J. Houska, Tribological properties and oxidation resistance of tungsten and tungsten nitride films at temperatures up to 500 °C, Tribol. Int. 132 (2019) 211–220.

[2] S.B. Ghantasala, S. Sharma, Magnetron sputtered thin films based on transition metal nitride: structure and properties, Phys. Status Solidi A 220 (2) (Jan. 2023) 2200229, https://doi.org/10.1002/pssa.202200229, issn: 1862-6300, 1862-6319. (visited on 08/03/2023).

[3] S. Ganguli, L. Chen, T. Levine, B. Zheng, M. Chang, Development of tungsten nitride film as barrier layer for copper metallization, J. Vac. Sci. Technol. B Microelectron. Nanometer Struct. Process. Measure. Phenom. 18 (1) (Jan. 2000) 237–241, https://doi.org/10.1116/1.591178, issn: 1071-1023. (visited on 11/21/2023).

[4] J.S. Becker, R.G. Gordon, Diffusion barrier properties of tungsten nitride films grown by atomic layer deposition from bis(tert-butylimido)bis(dimethylamido) tungsten and ammonia, Appl. Phys. Lett. 82 (14) (2003) 2239–2241, https://doi.org/10.1063/1.1565699.

[5] B. Wehring, F. Karakus, L. Gerlich, B. Lilienthal-Uhlig, M. Hecker, C. Leyens, Material screening for future diffusion barriers in Cu interconnects: modeling of binary and ternary metal alloys and detailed analysis of their barrier performance, J. Appl. Phys. 135 (21) (Jun. 2024), https://doi.org/10.1063/5.0211802 issn: 1089-7550. [Online]. Available: doi:10.1063/5.0211802.

[6] V. Tiron, I.-L. Velicu, C. Porosnicu, I. Burducea, P. Dinca, P. Malinský, Tungsten nitride coatings obtained by HiPIMS as plasma facing materials for fusion applications, Appl. Surf. Sci. 416 (2017) 878–884, https://doi.org/10.1016/j.apsusc.2017.04.183 (visited on 11/30/2022).

[7] K. Schmid, et al., Interaction of nitrogen plasmas with tungsten, Nucl. Fusion 50 (2) (2010) 025006, https://doi.org/10.1088/0029-5515/50/2/025006, issn: 0029-5515. (visited on 09/26/2023).

[8] L. Gao, et al., Interaction of deuterium plasma with sputter-deposited tungsten nitride films, Nucl. Fusion 56 (1) (Nov. 2015) 016004, https://doi.org/10.1088/0029-5515/56/1/016004, issn: 0029–5515. (visited on 09/27/2023).

[9] H.A. Wriedt, The N-W (nitrogen-tungsten) system, Bull. Alloy Phase Diagr. 10 (4) (Aug. 1989) 358–367, https://doi.org/10.1007/bf02877592, issn: 0197-0216. [Online]. Available: doi:10.1007/BF02877592.

[10] T. Polcar, N.M.G. Parreira, A. Cavaleiro, Tribological characterization of tungsten nitride coatings deposited by reactive magnetron sputtering, Wear 262 (5) (Feb. 2007) 655–665, https://doi.org/10.1016/j.wear.2006.07.010.

[11] C.C. Baker, S.I. Shah, Reactive sputter deposition of tungsten nitride thin films, J. Vac. Sci. Technol. A Vac. Surf. Films 20 (5) (2002) 1699, https://doi.org/10.1116/1.1498278.

[12] M.L. Addonizio, A. Castaldo, A. Antonaia, E. Gambale, L. Iemmo, Influence of process parameters on properties of reactively sputtered tungsten nitride thin films, J. Vac. Sci. Technol. A 30 (3) (May 2012) 031506, https://doi.org/10.1116/1.3698399, issn: 0734-2101. (visited on 11/30/2022).

[13] Y.G. Shen, Y.W. Mai, Structural studies of amorphous and crystallized tungsten nitride thin films by EFED, XRD and TEM, Appl. Surf. Sci. 167 (1) (2000) 59–68, https://doi.org/10.1016/S0169-4332(00)00508-0 (visited on 06/28/2023).

[14] Y.G. Shen, Y.W. Mai, D.R. McKenzie, Q.C. Zhang, W.D. McFall, W.E. McBride, Composition, residual stress, and structural properties of thin tungsten nitride films deposited by reactive magnetron sputtering, J. Appl. Phys. 88 (3) (2000) 1380–1388, https://doi.org/10.1063/1.373827 (visited on 11/30/2022).

[15] B. Wicher, et al., Chemical and structural characterization of tungsten nitride (WNx) thin films synthesized via gas injection magnetron sputtering technique, Vacuum 165 (2019) 266–273, https://doi.org/10.1016/j.vacuum.2019.04.020.

[16] A. Abdelhameed, W. Jacob, Deposition of thermally stable tungsten nitride thin films by reactive magnetron sputtering, Surf. Coat. Technol. 375 (2019) 701–707, https://doi.org/10.1016/j.surfcoat.2019.07.046, 0257-8972, https://www.sciencedirect.com/science/article/pii/S0257897219307820.

[17] A. Anders, A structure zone diagram including plasma-based deposition and ion etching, Thin Solid Films 518 (15) (2010) 4087–4090, https://doi.org/10.1016/j.tsf.2009.10.145.

[18] D. Lundin, J.T. Gudmundsson, T. Minea, High Power Impulse Magnetron Sputtering: Fundamentals, Technologies, Challenges and Applications, Elsevier, 2020, https://doi.org/10.1016/C2016-0-02463-4, 9780128124543.

[19] J.T. Gudmundsson, A. Anders, A. von Keudell, Foundations of physical vapor deposition with plasma assistance, Plasma Sources Sci. Technol. 31 (8) (Sep. 2022) 083001, https://doi.org/10.1088/1361-6595/ac7f53, issn: 0963-0252. (visited on 09/01/2023).

[20] G. Greczynski, S. Mráz, J.M. Schneider, L. Hultman, Metal-ion subplantation: a game changer for controlling nanostructure and phase formation during film growth by physical vapor deposition, J. Appl. Phys. 127 (18) (2020) 180901, https://doi.org/10.1063/1.5141342 (visited on 05/12/2023).

[21] A. Guillaumot, et al., Influence of substrate biasing on (Al, Ti)N thin films deposited by a hybrid HIPIMS/DC sputtering process, IEEE Trans. Plasma Sci. 38 (11) (2010) 3040–3045, https://doi.org/10.1109/tps.2010.2052931 [Online]. Available: doi:10.1109/TPS.2010.2052931.

[22] Y. Xu, G. Li, Y. Xia, Synthesis and characterization of super-hard AlCrTiVZr high-entropy alloy nitride films deposited by HiPIMS, Appl. Surf. Sci. 523 (Sep. 2020) 146529, https://doi.org/10.1016/j.apsusc.2020.146529, issn: 0169-4332. (visited on 11/30/2022).

[23] L. Zauner, et al., Reactive hipims deposition of Ti-Al-N: influence of the deposition parameters on the cubic to hexagonal phase transition, Surf. Coat. Technol. 382 (Jan. 2020) 125007, https://doi.org/10.1016/j.surfcoat.2019.125007, issn: 0257-8972. [Online]. Available: doi:10.1016/j.surfcoat.2019.125007.

[24] F. Cemin, G. Abadias, T. Minea, D. Lundin, Tuning high power impulse magnetron sputtering discharge and substrate bias conditions to reduce the intrinsic stress of TiN thin films, Thin Solid Films 688 (Oct. 2019) 137335, https://doi.org/10.1016/j.tsf.2019.05.054. A Special Issue "Thin Film Advances", Dedicated to the 75th Birth-day of Professor Joe Greene,. 0040-6090. (visited on 03/23/2023).

[25] H. Hajihoseini, M. Kateb, S. Ingvarsson, J. Gudmundsson, Effect of substrate bias on properties of HIPIMS deposited vanadium nitride films, Thin Solid Films 663 (2018) 126–130.

[26] M.M.S. Villamayor, et al., Low temperature (Ts/Tm < 0.1) epitaxial growth of HfN/MgO(001) via reactive hipims with metal-ion synchronized substrate bias, J. Vac. Sci. Technol. A Vac. Surf. Films 36 (6) (2018), https://doi.org/10.1116/1.5052702.

[27] A. Pshyk, I. Petrov, B. Bakhit, J. Lu, L. Hultman, G. Greczynski, Energy-efficient physical vapor deposition of dense and hard Ti-Al-W-N coatings deposited under industrial conditions, Mater. Des. 227 (Mar. 2023) 111753, https://doi.org/10.1016/j.matdes.2023.111753, issn: 0264-1275. [Online]. Available: doi:10.1016/j.matdes. 2023.111753.

[28] B.-S. Lou, I. Moirangthem, J.-W. Lee, Fabrication of tungsten nitride thin films by superimposed HiPIMS and MF system: effects of nitrogen flow rate, Surf. Coat. Technol. 393 (Jul. 2020) 125743, https://doi.org/10.1016/j.surfcoat.2020.125743, issn: 0257-8972. (visited on 11/30/2022).

[29] M.A. Raadu, I. Axnäs, J.T. Gudmundsson, C. Huo, N. Brenning, An ionization region model for high-power impulse magnetron sputtering discharges, Plasma Sources Sci. Technol. 20 (6) (Nov. 2011) 065007, https://doi.org/10.1088/0963-0252/20/6/065007, issn: 0963-0252. (visited on 01/17/2023).

[30] J.T. Gudmundsson, D. Lundin, N. Brenning, M.A. Raadu, C. Huo, T.M. Minea, An ionization region model of the reactive Ar/O_2 high power impulse magnetron sputtering discharge, Plasma Sources Sci. Technol. 25 (6) (Oct. 2016) 065004, https://doi.org/10.1088/0963-0252/25/6/065004, issn: 0963-0252. (visited on 07/12/2023).

[31] S.S. Babu, et al., Modeling of high power impulse magnetron sputtering discharges with tungsten target, Plasma Sources Sci. Technol. 31 (6) (Jun. 2022) 065009, https://doi.org/10.1088/1361-6595/ac774a, issn: 0963-0252. (visited on 10/21/2022).

[32] S. Suresh Babu, et al., High power impulse magnetron sputtering of tungsten: a comparison of experimental and modelling results, Plasma Sources Sci. Technol. 32 (3) (Mar. 2023) 034003, https://doi.org/10.1088/1361-6595/acc12f, issn: 1361-6595. [Online]. Available: doi:10.1088/1361-6595/acc12f.

[33] D. Vavassori, F. Mirani, F. Gatti, D. Dellasega, M. Passoni, Role of magnetic field and bias configuration on HIPIMS deposition of W films, Surf. Coat. Technol. 458 (Apr. 2023) 129343, https://doi.org/10.1016/j.surfcoat.2023.129343, issn: 0257-8972. [Online]. Available: doi:10.1016/j.surfcoat.2023.129343.

[34] S. Berg, T. Nyberg, Fundamental understanding and modeling of reactive sputtering processes, Thin Solid Films 476 (2) (2005) 215–230, https://doi.org/10.1016/j.tsf.2004.10.051, 0040-6090.

[35] B.C. Zheng, Z.L. Wu, B. Wu, Y.G. Li, M.K. Lei, A global plasma model for reactive deposition of compound films by modulated pulsed power magnetron sputtering discharges, J. Appl. Phys. 121 (17) (2017), https://doi.org/10.1063/1. 4977471.

[36] D. Lundin, J.T. Gudmundsson, N. Brenning, M.A. Raadu, T.M. Minea, A study of the oxygen dynamics in a reactive Ar/O_2 high power impulse magnetron sputtering discharge using an ionization region model, J. Appl. Phys. 121 (17) (2017), https://doi.org/10.1063/1.4977817.

[37] D. Dellasega, F. Mirani, D. Vavassori, C. Conti, M. Passoni, Role of energetic ions in the growth of fcc and ω crystalline phases in Ti films deposited by HiPIMS, Appl. Surf. Sci. 556 (2021) 149678, https://doi.org/10.1016/j.apsusc.2021.149678, issn: 0169-4332.

[38] T.H. de Keijser, J.I. Langford, E.J. Mittemeijer, A.B.P. Vogels, Use of the voigt function in a single-line method for the analysis of X-ray diffraction line broadening, J. Appl. Crystallogr. 15 (3) (1982) 308–314, https://doi.org/10.1107/s0021889882012035 [Online]. Available: doi:10.1107/S0021889882012035.

[39] A. Pandey, et al., Growth and morphological evolution of c-axis oriented aln films on Si (100) substrates by dc sputtering technique, in: AIP Conference Proceedings vol. 1953, 2018, p. 100028, https://doi.org/10.1063/1.5032964. Author(s). [Online]. Available: doi:10. 1063/1.5032964.

[40] M. Kumar, A. Kumar, A.C. Abhyankar, Influence of texture coefficient on surface morphology and sensing properties of W-doped nanocrystalline tin oxide thin films, ACS Appl. Mater. Interfaces 7 (6) (Feb. 2015) 3571–3580, https://doi.org/10.1021/am507397z, issn: 1944-8252. [Online]. Available: doi:10.1021/am507397z.

[41] M. Rudolph, D. Lundin, E. Foy, M. Debongnie, M.-C. Hugon, T. Minea, Influence of backscattered neutrals on the grain size of magnetron-sputtered TAN thin films, Thin Solid Films 658 (2018) 46–53, https://doi.org/10.1016/j.tsf.2018.05.027 [Online]. Available: doi:10.1016/j.tsf.2018.05.027.

[42] J.F. Ziegler, M. Ziegler, J. Biersack, Srim — the stopping and range of ions in matter (2010), Nucl. Instrum. Methods Phys. Res. B Beam Interact. Mater. Atoms 268 (11–12) (2010) 1818–1823, https://doi.org/10.1016/j.nimb.2010.02.091, doi:10.1016/j.nimb. 2010.02.091.

[43] B.C. Zheng, D. Meng, H.L. Che, M.K. Lei, On the pressure effect in energetic deposition of Cu thin films by modulated pulsed power magnetron sputtering: a

global plasma model and experiments, J. Appl. Phys. 117 (20) (2015), https://doi.org/10.1063/1.4921443 doi:10.1063/1.4921443.
[44] M.-Y. Song, H. Cho, G.P. Karwasz, V. Kokoouline, J. Tennyson, Cross sections for electron collisions with N_2, N_2*, and N_2^+, J. Phys. Chem. Ref. Data 52 (2) (2023) https://doi.org/10.1063/5.0150618.
[45] M. Rutigliano, F. Pirani, The sticking of N_2 on W(100) surface: an improvement in the description of the adsorption dynamics further reconciling theory and experiment, Molecules 28 (22) (2023) 7546, https://doi.org/10.3390/molecules28227546.
[46] D.A. King, M.G. Wells, Molecular beam investigation of adsorption kinetics on bulk metal targets: nitrogen on tungsten, Surf. Sci. 29 (2) (1972) 454–482, https://doi.org/10.1016/0039-6028(72)90232-4, doi: 10.1016/0039-6028(72)90232-4.
[47] M. Alducin, R. Díez Muinõ, H.F. Busnengo, A. Salin, Low sticking probability in the non-activated dissociation of N_2 molecules on W(110), J. Chem. Phys. 125 (14) (Oct. 2006), https://doi.org/10.1063/1.2355672 issn: 1089–7690. [Online]. Available: doi:10.1063/1.2355672.
[48] W. Möller, D. Güttler, Modeling of plasma-target interaction during reactive magnetron sputtering of tin, J. Appl. Phys. 102 (9) (Nov. 2007), https://doi.org/10.1063/1.2800262 issn: 1089-7550. [Online]. Available: doi:10.1063/1.2800262.
[49] A. Anders, Deposition rates of high power impulse magnetron sputtering: physics and economics, J. Vac. Sci. Technol. A 28 (4) (Jul. 2010) 783–790.
[50] B.M. Berger, et al., Transient effects during erosion of WN by deuterium ions studied with the quartz crystal microbalance technique, Nucl. Inst. Methods Phys. Res. B 382 (2016) 82–85.
[51] K. Dobes, P. Naderer, N. Lachaud, C. Eisenmenger-Sittner, F. Aumayr, Sputtering of tungsten by N^+ and N_2^+ ions: investigations of molecular effects, Phys. Scr. T145 (Dec. 2011) 014017, https://doi.org/10.1088/0031-8949/2011/t145/014017, issn: 1402-4896. [Online]. Available: doi:10.1088/0031-8949/2011/T145/014017.
[52] J. Ferron, E.V. Alonso, R.A. Baragiola, A. Oliva-Florio, Electron emission from molybdenum under ion bombardment, J. Phys. D Appl. Phys. 14 (9) (Sep. 1981) 1707–1720, https://doi.org/10.1088/0022-3727/14/9/018, issn: 1361-6463. [Online]. Available: doi:10.1088/0022-3727/14/9/018.
[53] N. Cook, R.B. Burtt, 1–17 keV positive ion-induced electron ejection from tungsten, molybdenum and vanadium, J. Phys. D. Appl. Phys. 8 (7) (1975) 800–811, https://doi.org/10.1088/0022-3727/8/7/012, 1361-6463.
[54] A. Hecimovic, C. Corbella, C. Maszl, W. Breilmann, A. von Keudell, Investigation of plasma spokes in reactive high power impulse magnetron sputtering discharge, J. Appl. Phys. 121 (17) (2017), https://doi.org/10.1063/1.4978348.
[55] R. Baragiola, E. Alonso, J. Ferron, A. Oliva-Florio, Ion-induced electron emission from clean metals, Surf. Sci. 90 (2) (Dec. 1979) 240–255, https://doi.org/10.1016/0039-6028(79)90341-8, issn: 0039-6028. [Online]. Available: doi:10.1016/0039-6028(79)90341-8.
[56] C. Huo, Y. Ji, S. Xie, R. Song, Q. Chen, Simulation results of the gas rarefaction and target ion evolution in a chopped high power impulse magnetron sputtering discharge, AIP Adv. 11 (12) (Dec. 2021) 125220.
[57] G. Buyle, D. Depla, K. Eufinger, R.D. Gryse, Calculation of the effective gas interaction probabilities of the secondary electrons in a dc magnetron discharge, J. Phys. D. Appl. Phys. 37 (12) (2004) 1639–1647.
[58] O. Shebanova, E. Soignard, P.F. Mcmillan, Compressibilities and phonon spectra of high-hardness transition metal-nitride materials, High Pressure Res. 26 (2) (2006) 87–97, https://doi.org/10.1080/08957950600765186.
[59] D. Dellasega, G. Merlo, C. Conti, C.E. Bottani, M. Passoni, Nanostructured and amorphous-like tungsten films grown by pulsed laser deposition, J. Appl. Phys. 112 (8) (2012), https://doi.org/10.1063/1.4761842 doi:10.1063/1.4761842.
[60] B. Braeckman, D. Depla, On the amorphous nature of sputtered thin film alloys, Acta Mater. 109 (2016) 323–329, https://doi.org/10.1016/j.actamat.2016.02.035 [Online]. Available: doi:10.1016/j.actamat.2016.02.035.
[61] J.A. Hofer, S. Bengio, S. Suárez, N. Haberkorn, Elucidating the role of disorder introduced by nitrogen in the superconducting properties of tungsten thin films, Mater. Adv. 4 (1) (2023) 150–156, https://doi.org/10.1039/d2ma00935h, issn: 2633-5409. [Online]. Available: doi:10.1039/D2MA00935H.
[62] A. Castaldo, E. Gambale, L. Iemmo, Thermal stability of sputtered tungsten nitrides for solar thermal applications, Appl. Sci. 12 (20) (2022) 10208, https://doi.org/10.3390/app122010208.
[63] C. Palacio, J. Sanz, J. Mart'ınez-Duart, Preferential sputtering effects in tantalum nitride thin films, Thin Solid Films 124 (3–4) (Feb. 1985) 243–247, https://doi.org/10.1016/0040-6090(85)90272-x, issn: 0040-6090. [Online]. Available: doi:10.1016/0040- 6090(85)90272-X.
[64] S. Guruvenket, G. Mohan Rao, Bias induced structural changes in tungsten nitride films deposited by unbalanced magnetron sputtering, Mater. Sci. Eng. B 106 (2) (2004) 172–176, https://doi.org/10.1016/j.mseb.2003.09.016, issn: 0921-5107. (visited on 05/11/2023).
[65] D. Vavassori, et al., Corrosion resistance of HIPIMS tungsten and tungsten-aluminium coatings in contact with liquid Sn, Surf. Coat. Technol. 494 (Oct. 2024) 131449, https://doi.org/10.1016/j.surfcoat.2024.131449, issn: 0257-8972. [Online]. Available: doi:10.1016/j.surfcoat.2024.131449.
[66] D.D. Kumar, N. Kumar, S. Kalaiselvam, S. Dash, R. Jayavel, Wear resistant superhard multilayer transition metal-nitride coatings, Surf. Interface Anal. 7 (2017) 74–82, https://doi.org/10.1016/j.surfin.2017.03.001 [Online]. Available: doi:10.1016/j.surfin.2017.03.001.
[67] H. Aghajani, M.S. Motlagh, Effect of temperature on surface characteristics of nitrogen ion implanted biocompatible titanium, J. Mater. Sci. Mater. Med. 28 (2) (Jan. 2017), https://doi.org/10.1007/s10856-016-5843-x issn: 1573-4838. [Online]. Available: doi:10.1007/s10856-016-5843-x.
[68] C. Huo, D. Lundin, J.T. Gudmundsson, M.A. Raadu, J.W. Bradley, N. Brenning, Particle-balance models for pulsed sputtering magnetrons, J. Phys. D Appl. Phys. 50 (35) (Aug. 2017) 354003, https://doi.org/10.1088/1361-6463/aa7d35, issn: 1361-6463. [Online]. Available: doi:10.1088/1361-6463/aa7d35.
[69] J.T. Gudmundsson, J. Fischer, B.P. Hinriksson, M. Rudolph, D. Lundin, Ionization region model of high power impulse magnetron sputtering of copper, Surf. Coat. Technol. 442 (Jul. 2022) 128–189, https://doi.org/10.1016/j.surfcoat.2022.128189. Special Issue of Surface and Coatings Technology Celebrating the Pioneering Research Career of Professor Allan Matthews in the Field of "Plasma-based Surface Engineering". issn: 0257-8972. (visited on 08/02/2023).
[70] A. Butler, N. Brenning, M.A. Raadu, J.T. Gudmundsson, T. Minea, D. Lundin, On three different ways to quantify the degree of ionization in sputtering magnetrons, Plasma Sources Sci. Technol. 27 (10) (Oct. 2018) 105005, https://doi.org/10.1088/1361-6595/aae05b, issn: 1361-6595. [Online]. Available: doi:10.1088/1361-6595/aae05b.
[71] A.P. Ehiasarian, A. Vetushka, Y.A. Gonzalvo, G. S'afr'an, L. Sz'ekely, P.B. Barna, Influence of high power impulse magnetron sputtering plasma ionization on the microstructure of tin thin films, J. Appl. Phys. 109 (10) (2011), https://doi.org/10.1063/1.3579443 [Online]. Available: doi:10.1063/1.3579443.
[72] G. Greczynski, I. Zhirkov, I. Petrov, J.E. Greene, J. Rosen, Time evolution of ion fluxes incident at the substrate plane during reactive high-power impulse magnetron sputtering of groups IVB and VIB transition metals in Ar/N_2, J. Vac. Sci. Technol. A 36 (2) (2018), https://doi.org/10.1116/1.5016241.
[73] I. Petrov, P.B. Barna, L. Hultman, J.E. Greene, Microstructural evolution during film growth, J. Vac. Sci. Technol. A Vac. Surf. Films 21 (5) (Sep. 2003) S117–S128, https://doi.org/10.1116/1.1601610, issn: 1520-8559. [Online]. Available: doi:10.1116/1.1601610.
[74] A. Macrelli, et al., Nanostructure and phase engineering of manganese oxide thin films grown by pulsed laser deposition: a Raman and XRD study, Phys. Rev. Mater. 7 (8) (2023), https://doi.org/10.1103/physrevmaterials.7.083403 doi:10.1103/PhysRevMaterials.7.083403.
[75] S. Lien, H. Mao, B. Wu, R. Horng, D. Wuu, Incubation effects upon polycrystalline silicon on glass deposited by hot-wire CVD, Chem. Vap. Depos. 13 (5) (2007) 247–252, https://doi.org/10.1002/cvde.200606576 [Online]. Available: doi:10.1002/cvde.200606576.